DOI: 10.22055/JACM.2018.25097.1228

J. Appl. Comput. Mech., 5(1) (2019) 113-127
DOI: 10.22055/JACM.2018.25097.1228

ISSN: 2383-4536
jacm.scu.ac.ir

M&MoCS

Shahid Chamran University of Ahvaz

Journal of Applied and Computational Mechanics

Research Paper

Topology Optimization of the Thickness Profile of Bimorph Piezoelectric Energy Harvesting Devices

Breno Vincenzo de Almeida[1], Renato Pavanello[2]

[1] School of Mechanical Engineering, Department of Computational Mechanics, University of Campinas
Cidade Universitria Zeferino Vaz - Barao Geraldo, 13083-970, Campinas, Sao Paulo, Brazil, brenodealmeida4@gmail.com
[2] School of Mechanical Engineering, Department of Computational Mechanics, University of Campinas
Cidade Universitria Zeferino Vaz - Barao Geraldo, 13083-970, Campinas, Sao Paulo, Brazil, pava@fem.unicamp.br

Received February 22 2018; Revised April 26 2018; Accepted for publication May 30 2018.
Corresponding author: Breno Vincenzo de Almeida, brenodealmeida4@gmail.com

Abstract. Due to developments in additive manufacturing, the production of piezoelectric materials with complex geometries is becoming viable and enabling the manufacturing of thicker harvesters. Therefore, in this study a piezoelectric harvesting device is modelled as a bimorph cantilever beam with a series connection and an intermediate metallic substrate using the plane strain hypothesis. On the other hand, the thickness of the harvester's piezoelectric material is structurally optimized using a discrete topology optimization method. Moreover, different optimization parameters are varied to investigate the algorithm's convergence. The results of the optimization are presented and analyzed to examine the influence of the harvester's geometry and its different substrate materials on the harvester's energy conversion efficiency.

Keywords: Piezoelectric; Harvester; Structural optimization.

1. Introduction

Piezoelectric materials generate an electric field when subjected to a mechanical load due to a phenomenon called the direct piezoelectric effect, discovered by Pierre and Jacques Curie in 1880. Lippmann [1] then used thermodynamic principles to obtain the inverse piezoelectric effect, in which an electric field applied to a piezoelectric material and deformed it; this effect was later experimentally demonstrated by the Curie brothers in 1881. Many naturally occurring piezoelectric materials were discovered in the early XX century, such as topaz, quartz, and Rochelle salt, but they did not have properties suited for engineering applications. It was only later that artificial piezoelectric ceramics with sufficiently large coupling properties were developed and utilized for energy harvesting applications such as lead zirconate titanate (PZT) [2].

Close to the end of the XX century, the methods used to discretize a continuum, such as Finite Element Analysis (FEA), were becoming progressively more elaborate due to increasing breakthroughs in computation and were adapted to be used in the modeling and optimizing the piezoelectric phenomena for transducing and then energy harvesting [3]. Therefore, topology optimization techniques utilized such prevailed computational discretization methods such as the Solid Isotropic Material with Penalization (SIMP) method [4] and the Evolutionary Structural Optimization (ESO) method [5]. These developments were especially employed to solve compliance minimization and natural frequency maximization related problems for macro- as well as micro-scale structures [6].

Structural optimization procedures have also been used in various multi-physical problems such as the frequency response of fluid-structure systems [7], the automotive muffler acoustic topology optimization [8] and the frequency maximization problems for acoustic-structure interactions [9]. More closely related to the present research, numerous studies have been written for the topology optimization of piezoelectric materials and its applications as follows: Sigmund *et. al.* [10] optimized the design

Published online: January 07 2019

of 1-3 piezocomposites for piezoelectric transducers, as did Silva *et. al.* [11] but with a homogenization approach while Donoso and Sigmund [12] considered optimal design problems for active damping. Furthermore, advances were made in the area of energy harvesting devices: Zheng *et. al.* [13] focused on optimizing a three-dimensional piezoelectric harvester subjected to static loading conditions using a finite element (FE) mesh while Noh and Yoon [14] further developed this by considering dynamic as well as static loads and applying the SIMP model and using different penalization factors for each of the piezoelectric material's physical properties. Lin *et. al.* [15] also used different penalization factors for a three-dimensional FE mesh using one element per layer in the thickness direction by considering base vibrations and optimizing the topology for a range of frequencies instead of a single input frequency. Moreover, Kiyono *et. al.* [16] optimized a piezoelectric harvester modelled with a multilayered shell element.

Most of these piezoelectric topology optimization studies used the SIMP method for the optimization problem and to the best of the authors' knowledge, only performed topology optimization of the piezoelectric layers modelled as plate [15], shell [16] .Moreover, they used a three-dimensional model with only one or two elements per layer in the thickness direction [13,14] while a FE analysis of the optimal topology for the thickness direction is seldom done, with the exception of Donoso and Sigmund [12], who optimized the thickness of a piezoelectric energy harvesting device analytically by not enabling void regions inside the piezoelectric domain. This can be attributed to limitations to produce more complex piezoelectric structures due to restrictions in the fabrication process of piezoelectric materials, which cannot be created though conventional manufacturing techniques such as etching and dicing, especially for piezoelectric ceramics [17].

There have been significant developments in the production methods of these materials, especially with the improvement of Additive Manufacturing (AM) techniques. For piezocomposite materials, such as polyvinylidene fluoride (PVDF), there are techniques such as electron beam lithography, soft lithography, electrospinning, and contact printing, among others. But these methods are not quite suitable for generating more complex multilayered piezoelectric polymer architectures [18]. Kim *et. al.* [18] developed a stereolithographic (SLA) method, capable of fabricating elaborate piezocomposite structures by using a photoliable piezoelectric polymer solution which solidifies when exposed to light. More recently, Bodkhe *et. al.* [19] developed a one-step method of generating complex piezocomposite structures, also with PVDF, by means of a solvent evaporation technique, conferring piezoelectric properties without the need of subsequent poling or secondary treatments. Chen *et. al.* [17] focused on developing an AM process capable of generating more sophisticated structures with environmentally friendly piezoelectric ceramics, i.e., without lead, with barium titanate nanoparticles, using Mask-Image-Projection based Stereolithography (MIP-SL) technology. Due to these advancements in piezoelectric material AM techniques, it is of interest to study the topology optimization of piezoelectric harvesting devices in the thickness direction.

Therefore, in this study, the harvester is modelled as a bimorph two-dimensional beam under the plane strain hypothesis and as a section of a three-dimensional beam, as shown in Fig. 1. The beam is composed of two piezoelectric layers of opposing polarities (series connection) and an intermediate metallic substrate under open-circuit conditions.

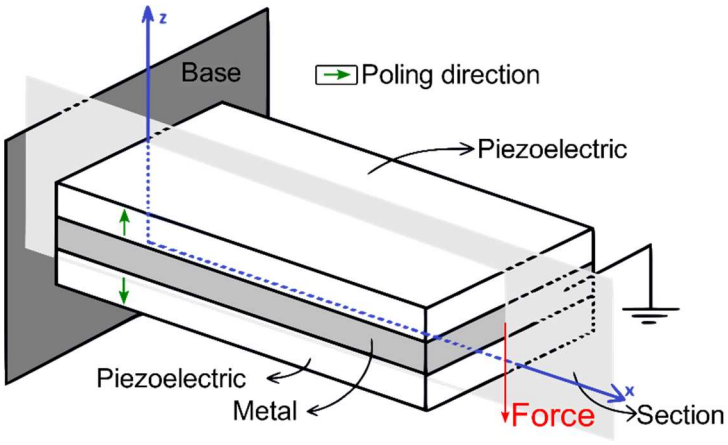

Fig. 1. Piezoelectric harvester model

The FE model and the subsequent topology optimization procedure are shown in section 2. The objective function consists on minimizing the inverse ratio of the output electric energy by the input force work [13,14]. The force is considered static, which yields results comparable to dynamic excitations with input frequency lower than the first resonance frequency; since the vibration mode is similar to the static deformed shape. The BESO method is then used to optimize the topology of the piezoelectric material of the harvester by considering a static load on the free end of the beam and a fixed topology for the metallic substrate. The sensitivities of a minimization problem are derived and different penalization parameters are used for each of the piezoelectric material's stiffness [14] in order to find a better convergence.

Finally, in sections 3 to 5, numerical results are displayed and the influence of the harvester's geometry and the substrate's material on the objective function are investigated. A conclusion summarizing the results is presented in section 6.

2. Model formulation and optimization Problem

By simplifying the constitutive equations of piezoelectric phenomena using the plane-strain hypothesis and using the linear Hamilton principle with the known linear stress-displacement and electric field-electric potential relations, we can obtain the

element piezoelectric stiffness matrix, which when assembled, results in the governing global equilibrium equation shown in Eq. (1) [20,21].

$$\begin{bmatrix} \mathbf{K}_{uu} & \mathbf{K}_{\phi u}^{T} \\ \mathbf{K}_{\phi u} & -\mathbf{K}_{\phi\phi} \end{bmatrix} \begin{bmatrix} \boldsymbol{u} \\ \boldsymbol{\phi} \end{bmatrix} = \begin{bmatrix} \boldsymbol{F} \\ \boldsymbol{Q} \end{bmatrix} , \tag{1}$$

In Eq. (1), $\boldsymbol{u}$, $\boldsymbol{\phi}$, $\boldsymbol{F}$, and $\boldsymbol{Q}$ are the nodal displacements, electric potential, force, and charge vectors, respectively, while $\mathbf{K}_{uu}$, $\mathbf{K}_{\phi u}$, and $\mathbf{K}_{\phi\phi}$ are the global mechanical stiffness, piezoelectric, and dielectric matrices, respectively. Furthermore, the corresponding matrices are calculated element-wise as shown in Eq. (2).

$$\begin{aligned} \mathbf{K}_{uu}^{e} &= \int_{\Omega_e} \mathbf{B}_u^T \mathbf{c}^E \mathbf{B}_u d\Gamma^e \\ \mathbf{K}_{\phi u}^{e} &= \int_{\Omega_e} \mathbf{B}_\phi^T \mathbf{e} \mathbf{B}_u d\Gamma^e \\ \mathbf{K}_{\phi\phi}^{e} &= \int_{\Omega_e} \mathbf{B}_\phi^T \boldsymbol{\varepsilon}^S \mathbf{B}_\phi d\Gamma^e \end{aligned} , \tag{2}$$

In Eq. (2), the superscript e indicates an element, $\mathbf{B}_u$ and $\mathbf{B}_\phi$ are the first order derivatives of the shape functions used to interpolate the displacements and electric potential, respectively, $\mathbf{c}^E$ is the elastic matrix for zero electric potential, $\mathbf{e}$ is the piezoelectric strain matrix, $\boldsymbol{\varepsilon}^S$ is the dielectric matrix for zero strain and Ω represents the element area. The plane-strain hypothesis is adopted and Linear isoparametric four-node elements were used for the FE procedure.

In the present study, the main piezoelectric material used is PZT-4. Considering that this material is polarized along the z-direction and according to the Institute of Electrical and Electronics Engineers' [20] standard, the following property matrices are provided:

$$\mathbf{e} = \begin{bmatrix} 0 & 0 & -5.2 \\ 0 & 0 & -5.2 \\ 0 & 0 & 15.1 \\ 0 & 12.7 & 0 \\ 12.7 & 0 & 0 \\ 0 & 0 & 0 \end{bmatrix} C/m^2 , \tag{3}$$

$$\mathbf{c}^E = \begin{bmatrix} 1.390 & 0.778 & 0.743 & 0 & 0 & 0 \\ 0.778 & 1.390 & 0.743 & 0 & 0 & 0 \\ 0.743 & 0.743 & 1.154 & 0 & 0 & 0 \\ 0 & 0 & 0 & 0.256 & 0 & 0 \\ 0 & 0 & 0 & 0 & 0.256 & 0 \\ 0 & 0 & 0 & 0 & 0 & 0.306 \end{bmatrix} 10^2 GPa , \tag{4}$$

$$\boldsymbol{\varepsilon}^{\mathrm{S}} = \begin{bmatrix} 6.45 & 0 & 0 \\ 0 & 6.45 & 0 \\ 0 & 0 & 5.62 \end{bmatrix} \mathrm{nF/m} , \tag{5}$$

Note that in this study, only a series connection of the piezoelectric sections of the energy harvesting device is analyzed, that is, the piezoelectric layers are modelled as having inverse poling directions. The top piezoelectric layer has a poling direction in 3 (or z), as shown in Fig. 1. Therefore, the bottom layer has a poling direction in -3 (or $-z$) in the global coordinate system, which can be achieved by multiplying the piezoelectric matrix in Eq. (3) by -1.

Initially, the only boundary conditions applied are the clamped conditions in the left-hand side (zero displacements) and the electrodes that cover the substrate are grounded (zero electric potential). These boundary conditions are similar to open-circuit conditions. After obtaining the optimization convergence and final topology under these considerations, equipotential voltage boundary conditions are applied in the top as well as bottom nodes (coupling voltage constraints) and the optimization procedure is done once again, while still considering the open-circuit condition. This coupling constraint is applied by tracking the solid-void boundary and by means of a Lagrange matrix $\boldsymbol{\Lambda}$ through expanding Eq. (1), which is simplified to $\mathbf{K}_g \boldsymbol{u}_g = \boldsymbol{F}_g$ in Eq. (6) [21].

$$\begin{bmatrix} \mathbf{K}_g & \boldsymbol{\Lambda}^T \\ \boldsymbol{\Lambda} & 0 \end{bmatrix} \begin{bmatrix} \boldsymbol{u}_g \\ \boldsymbol{l} \end{bmatrix} = \begin{bmatrix} \boldsymbol{F}_g \\ \mathbf{0} \end{bmatrix} , \tag{6}$$

In Eq. (6), $\boldsymbol{l}$ is a vector that when pre-multiplied by $\boldsymbol{\Lambda}^T$, it represents the internal forces needed to guarantee the electrode coupling constraints and is not used for the subsequent topology optimization calculations.

Next, the BESO method is used to find the optimal harvester topology considering the inverse energy conversion factor, as shown in Eq. (7). The soft-kill BESO method is used, in which a material interpolation scheme with penalization for intermediate densities is considered for three stiffnesses that shown in Eq. (2). The design variables of this optimization problem are element densities, represented by x_i or in the vector form, $\boldsymbol{x}$, which have the value of 1 for solid elements and the value of x_{min} (a small number) for void elements. The main advantages of using this topology optimization method are that it is a sensitivity- base method, it uses discrete variables, and it is relatively simple to implement [6]. The mesh dependency and the checkerboard pattern are avoided by the application of a filter in each iteration [6]. Since the BESO method yields well defined solid-void boundaries during all iterations of the optimization procedure, it is significantly well suited for the proposed topology optimization of the thickness profile of piezoelectric energy harvesters. Because the boundaries where the electrodes are applied can be readily tracked and the Lagrange coupling matrix $\boldsymbol{\Lambda}$ from Eq. (6) can be easily built.

The piezoelectric harvester's optimization algorithm solves the following minimization problem [13,14]:

$$\begin{aligned} &minimize && \zeta = 1 + \frac{\Pi^S}{\Pi^{\mathrm{E}}} \\ &subject\ to && V^* - \sum_{i=1}^{N} V_i x_i = 0 \\ & && x_i = x_{min} \ \text{or} \ x_i = 1 \\ & && i = 1, \ldots, \text{number of elements} \end{aligned} \quad , \tag{7}$$

In Eq. (7), ζ is the inverse conversion factor of the electric energy Π^{E} divided by the work of the applied force which is calculated as the sum of the electrical and the strain energy Π^S. Π^S and Π^{E} are calculated as shown in Eq. (8) using the nodal mechanical displacements $\boldsymbol{u}$ and the nodal voltages $\boldsymbol{\phi}$ as provided in Eq. (1), without electrodes, or in Eq. (6), with electrodes connected in series.

$$\Pi^S = \frac{1}{2}\boldsymbol{u}^T\mathbf{K}_{uu}\boldsymbol{u} \qquad and \qquad \Pi^E = \frac{1}{2}\,\boldsymbol{\phi}^T\mathbf{K}_{\phi\phi}\boldsymbol{\phi} \ , \tag{8}$$

Eq. (9) shows how the element sensitivities α_i are calculated by differentiating the objective function ζ with respect to the i-th element's density x_i:

$$\alpha_i = \frac{\partial \zeta}{\partial x_i} = \frac{1}{\Pi^E}\frac{\partial \Pi^S}{\partial x_i} - \frac{\Pi^S}{(\Pi^E)^2}\frac{\partial \Pi^E}{\partial x_i} \ , \tag{9}$$

The adjoint method is used to determine the derivative of the strain energy with respects to the i-th element's density [13,14]:

$$\Pi^S = \frac{1}{2}\boldsymbol{u}^T\mathbf{K}_{uu}\boldsymbol{u} + \boldsymbol{\lambda}_1^T\left(\mathbf{K}_{uu}\boldsymbol{u} + \mathbf{K}_{\phi u}^T\boldsymbol{\phi} - \mathbf{F}\right) + \boldsymbol{\mu}_1^T\left(\mathbf{K}_{\phi u}\boldsymbol{u} - \mathbf{K}_{\phi\phi}\boldsymbol{\phi}\right) \ , \tag{10}$$

In Eq. (10), $\boldsymbol{\lambda}_1$ and $\boldsymbol{\mu}_1$ are the adjoint terms. Since the harvester is not subjected to any external charge and is optimized in open-circuit condition, $\boldsymbol{Q} = \mathbf{0}$ [13].

Therefore, differentiating the strain energy of Eq. (10) with respect to the i-th element's density x_i leads to

$$\begin{aligned} \frac{\partial \Pi^S}{\partial x_i} = &\left(\boldsymbol{u}^T\mathbf{K}_{uu} + \boldsymbol{\lambda}_1^T\mathbf{K}_{uu} + \boldsymbol{\mu}_1^T\mathbf{K}_{\phi u}\right)\frac{\partial \boldsymbol{u}}{\partial x_i} + \left(\boldsymbol{\lambda}_1^T\mathbf{K}_{\phi u}^T - \boldsymbol{\mu}_1^T\mathbf{K}_{\phi\phi}\right)\frac{\partial \boldsymbol{\phi}}{\partial x_i} + \frac{1}{2}\boldsymbol{u}^T\frac{\partial \mathbf{K}_{uu}}{\partial x_i}\boldsymbol{u} \\ &+ \frac{\partial \boldsymbol{\lambda}_1^T}{\partial x_i}\left(\mathbf{K}_{uu}\boldsymbol{u} + \mathbf{K}_{\phi u}^T\boldsymbol{\phi} - \mathbf{F}\right) + \frac{\partial \boldsymbol{\mu}_1^T}{\partial x_i}\left(\mathbf{K}_{\phi u}\boldsymbol{u} - \mathbf{K}_{\phi\phi}\boldsymbol{\phi}\right) \\ &+ \boldsymbol{\lambda}_1^T\left(\frac{\partial \mathbf{K}_{uu}}{\partial x_i}\boldsymbol{u} + \frac{\partial \mathbf{K}_{\phi u}^T}{\partial x_i}\boldsymbol{\phi} - \frac{\partial \boldsymbol{F}}{\partial x_i}\right) + \boldsymbol{\mu}_1^T\left(\frac{\partial \mathbf{K}_{\phi u}}{\partial x_i}\boldsymbol{u} - \frac{\partial \mathbf{K}_{\phi\phi}}{\partial x_i}\boldsymbol{\phi}\right) \end{aligned} \tag{11}$$

In Eq. (11), the external force $\boldsymbol{F}$ is constant with respects to x_i, thus its derivative is null, and the terms multiplied by $\partial\boldsymbol{\lambda}_1^T/\partial x_i$and $\partial\boldsymbol{\mu}_1^T/\partial x_i$ are also null, due to the equilibrium Eq. (1) and because $\boldsymbol{Q} = \mathbf{0}$. Moreover, the terms multiplying by $\partial\boldsymbol{u}/\partial x_i$ and $\partial\boldsymbol{\phi}/\partial x_i$ are equaled to zero using the adjoint method and the following linear system is obtained:

$$\begin{bmatrix} \mathbf{K}_{uu} & \mathbf{K}_{\phi u}^T \\ \mathbf{K}_{\phi u} & -\mathbf{K}_{\phi\phi} \end{bmatrix}\begin{bmatrix} \boldsymbol{\lambda}_1 \\ \boldsymbol{\mu}_1 \end{bmatrix} = \begin{bmatrix} -\mathbf{K}_{uu}\boldsymbol{u} \\ \mathbf{0} \end{bmatrix} \ , \tag{12}$$

The adjoint terms calculated in Eq. (12) can then be used in Eq. (11) and the complete sensitivity for the strain energy is:

$$\frac{\partial \Pi^S}{\partial x_i} = \left(\frac{1}{2}\boldsymbol{u}^T + \boldsymbol{\lambda}_1^T\right)\frac{\partial \mathbf{K}_{uu}}{\partial x_i}\boldsymbol{u} + \boldsymbol{\lambda}_1^T\frac{\partial \mathbf{K}_{\phi u}^T}{\partial x_i}\boldsymbol{\phi} + \boldsymbol{\mu}_1^T\frac{\partial \mathbf{K}_{\phi u}}{\partial x_i}\boldsymbol{u} - \boldsymbol{\mu}_1^T\frac{\partial \mathbf{K}_{\phi\phi}}{\partial x_i}\boldsymbol{\phi} \quad , \tag{13}$$

Similar to in Eqs. (12) and (13), to find the adjoint terms $\boldsymbol{\lambda}_2$ and $\boldsymbol{\mu}_2$ for the sensitivity of the electric energy, the following linear system is solved:

$$\begin{bmatrix} \mathbf{K}_{uu} & \mathbf{K}_{\phi u}^T \\ \mathbf{K}_{\phi u} & -\mathbf{K}_{\phi\phi} \end{bmatrix}\begin{bmatrix} \boldsymbol{\lambda}_2 \\ \boldsymbol{\mu}_2 \end{bmatrix} = \begin{bmatrix} \mathbf{0} \\ -\mathbf{K}_{\phi\phi}\boldsymbol{\phi} \end{bmatrix} \quad , \tag{14}$$

The sensitivity of the electric energy with respect to the i-th element's density can then be calculated using the adjoint terms:

$$\frac{\partial \Pi^E}{\partial x_i} = \frac{1}{2}\boldsymbol{\phi}^T\frac{\partial \mathbf{K}_{\phi\phi}}{\partial x_i}\boldsymbol{\phi} + \boldsymbol{\lambda}_2^T\frac{\partial \mathbf{K}_{uu}}{\partial x_i}\boldsymbol{u} + \boldsymbol{\lambda}_2^T\frac{\partial \mathbf{K}_{\phi u}^T}{\partial x_i}\boldsymbol{\phi} + \boldsymbol{\mu}_2^T\frac{\partial \mathbf{K}_{\phi u}}{\partial x_i}\boldsymbol{u} - \boldsymbol{\mu}_2^T\frac{\partial \mathbf{K}_{\phi\phi}}{\partial x_i}\boldsymbol{\phi} \quad , \tag{15}$$

To be able to calculate Eqs. (13) and (15), the remaining terms have to be defined, namely the derivative of the stiffness matrices with respect to the elements densities. Therefore, a material interpolation scheme similar to the SIMP method is used by considering one penalization value for each of the stiffness components, as done by Noh & Yoon [14]. Therefore, the element stiffness matrices are as follows:

$$\mathbf{K}_{uu}^e = x^{p_1}\mathbf{K}_{uu}^e \qquad \mathbf{K}_{\phi u}^e = x^{p_2}\mathbf{K}_{\phi u}^e \qquad \mathbf{K}_{\phi\phi}^e = x^{p_3}\mathbf{K}_{\phi\phi}^e \quad , \tag{16}$$

In Eq. (16), p_1 is the penalization factor for the mechanical stiffness matrix, p_2 stands for the piezoelectric stiffness matrix, p_3 indicates the electrical one and $0 < x \leq 1$. The penalization factors are introduced to improve the optimization algorithm's convergence.

Additionally, extra weight factors w_S and w_E were used in Eq. (9) for the mechanical and electrical contributions to the sensitivity, respectively, to further stabilize the convergence:

$$\alpha_i = w_S\frac{1}{\Pi^E}\frac{\partial \Pi^S}{\partial x_i} - w_E\frac{\Pi^S}{(\Pi^E)^2}\frac{\partial \Pi^E}{\partial x_i} \tag{17}$$

Figure 2 shows a flow chart of the soft-kill BESO optimization procedure. The first step is to determine the starting topology, the boundary constraints, and the properties of each material. A loop is then initialized, where a FE analysis of the harvester is done to obtain the nodal displacements and nodal electric potentials using Eqs. (1) or (6). Next, a sensitivity calculation is performed (calculating the sensitivities as shown in Eq. (17)) to determine which elements should be solid and which ones should become void to minimize the objective function. To avoid the mesh dependency and the checkerboard pattern, a filter is applied. Based on the evolutionary ratio and the maximum permissible variation of solid to void and void to solid elements of the optimization procedure, the topology is then reconfigured according to the sensitivity analysis, i.e., a certain number of solid elements which contribute negatively to the objective function become void, and a number of void elements which contribute positively to the objective function become solid. This number is limited per iteration so as to avoid instabilities.

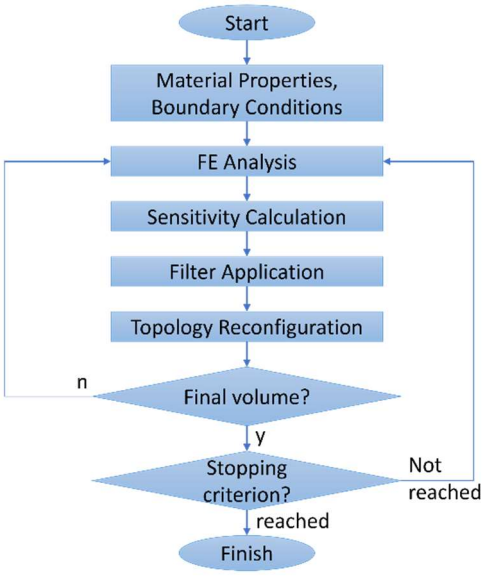

Fig. 2. BESO flow chart

Only the piezoelectric elements are considered as the design domain. Therefore, the metallic substrate is not taken during the filter application. Additionally, the initial design consists of 100% solid elements. The iterative procedure continues until the final volume is reached and the stopping criterion is met. The stopping criterion is determined by the objective functions' variability during in the last 10 iterations, which has to be lower than a very small value (e.g., 10^{-6}).

Therefore, a multiparameter (p_1, p_2, p_3, w_S, and w_E) algorithm has been proposed. It was provided using Matlab. In the next sections, analyses of the influence of the penalization factors, the harvester's geometry and the material properties are presented to study the topology optimization of the piezoelectric harvesting device's thickness profile.

3. Numerical results and discussion

Figure 3 illustrates the longitudinal section of the piezoelectric harvester which is optimized under different considerations in the next sections. The left-hand side of the beam is clamped and a force F is applied to the free end (right-hand side). The metallic substrate is represented in gray and the two white layers are made out of piezoelectric material with inverse polarities. The length is L, the thickness is H, and the substrate has a thickness equal to a fraction β of the total thickness ($0 < \beta < 1$). The results for both with and without equipotential boundary constraints are shown.

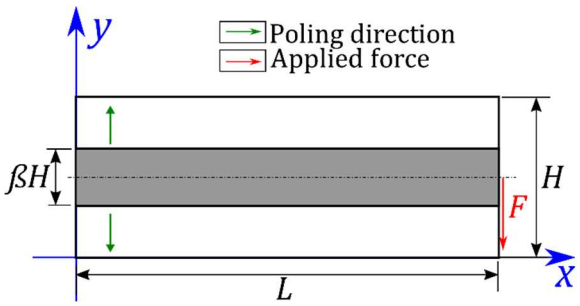

Fig. 3. Piezoelectric harvester two-dimensional section

3.1 Example 1: Bimorph harvester

As a first example, the soft-kill BESO iterative procedure explained beforehand was applied to optimize the topology of a bimorph piezoelectric harvester composed of a steel substrate, with the elasticity constant of $200GPa$ and the Poisson coefficient of 0.29, and the piezoelectric domain of PZT-4. The initial geometry of the harvester is set as $L = 100mm$, $H = 40mm$, and $\beta = 20\%$ ($\beta H = 8mm$). The force is $F = 100N$.

The design domain consists exclusively of the piezoelectric elements. The optimization is done with a 7200-element mesh (120 by 60). The initial volume is completely full and the final volume was 55% of the initial one. The evolutionary ratio ER was 2%, the density value for the void elements was 1%, and the maximum addition ratio AR was 1%. Additionally, the filter has a radius equal to $8mm$. The results are displayed in Fig. 4.

The sensitivity weight factors were $w_S = 60\%$ and $w_E = 40\%$, and the chosen penalization factors were $p_1 = 3$, $p_2 = 2$, and $p_3 = 1$.

In Fig. 4a, the convergence curve is shown in red, which is relatively smooth, and displays a 15.42% decrease of the objective function since the inverse conversion factor ζ from Eq. (7) changed from 7.39 to 6.25. The final topology is shown in Fig. 4b.

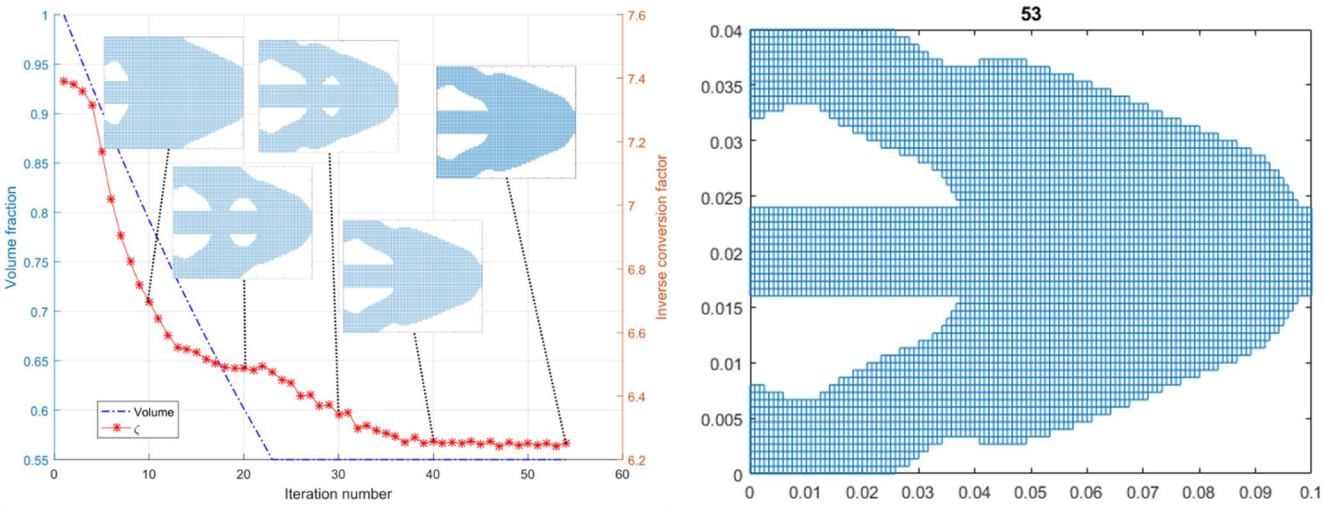

(a) Convergence curve **(b)** Final topology

Fig. 4. Topology optimization results for the piezoelectric harvester described in section 3

An identical analysis was done for the harvester with equipotential voltage constraints, and the results are displayed in Fig. 5. The non-grounded electrodes are displayed as red lines in Fig. 5b. The grounded electrodes are glued to the metallic substrate.

Considering an applied force of $F = 1N$, the harvester shown in Fig. 5 has an open circuit voltage output of $33.65\,mV$. It can be seen in Fig. 5a that the application of the equipotential boundary condition makes the optimization procedure unstable during the initial iterations. This may be attributed to the fact that the initial topology optimization volume is 100% of the design domain and the equipotential boundary condition artificially increases the sensitivity number of the elements in the upper-right and lower-right regions of the design domain, thus contributing to its instability. After the removal of the aforementioned nodes, the algorithm stabilizes. The final topology reached is similar to that of Fig. 4b, with the exception of a void region in the middle-right section of the harvester.

The inverse conversion factor decreases from 8.68 to 7.01, which corresponds to a 19.20% reduction of the objective function. Although the percentage reduction is greater, the additional constraint increases the inverse conversion factor, which means the harvester from Fig. 5 is less efficient than the one from Fig. 4 in transforming the input force's work to electrical energy.

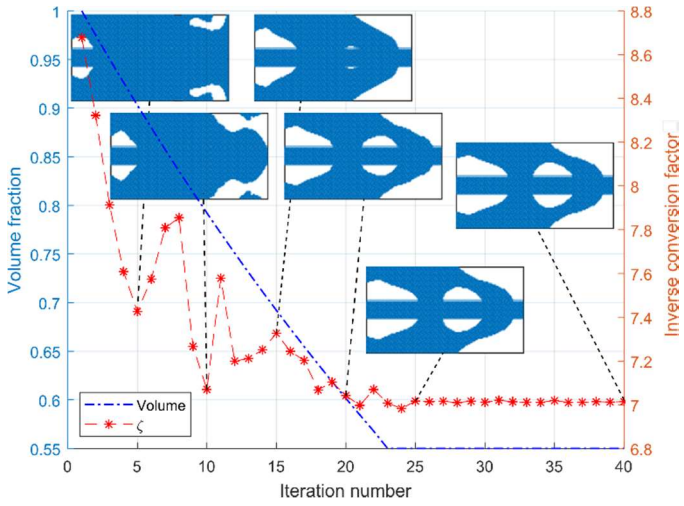

(a) Convergence curve

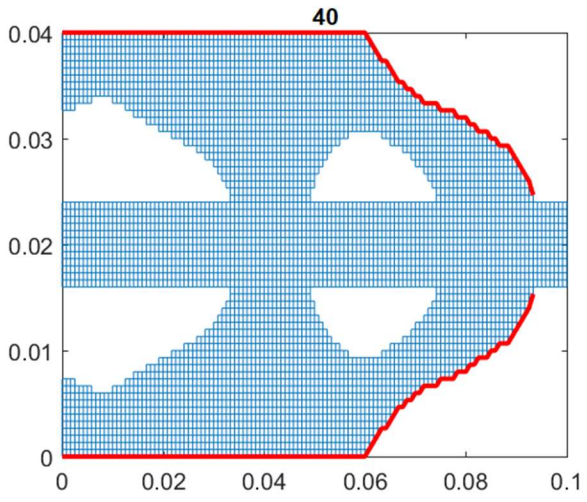

(b) Final topology. The red lines are the non-grounded electrodes

Fig. 5. Topology optimization results for the piezoelectric harvester described in section 3 considering equipotential constraints

To the best of the authors' knowledge, the results displayed in this example cannot be exactly compared to other results in literature since the thickness optimization of a piezoelectric harvester is not commonplace. The results found in this article can be compared approximately to results found for harvesters subjected to low frequency harmonic excitations since the first frequency's vibration mode is similar to that of the static excitation. By comparing Figs. 4b and 5b to Fig. 7a of Donoso and Sigmund [12], in which the optimized topology is shown for a harvester subjected to a force on its free end with a very small excitation frequency of $f = 1.9$ Hz, it can be observed that the algorithms both tend to put material in the left hand-side of the design domain, especially in the uppermost and lowermost regions. This is understandable since these regions have greater strain contributing significantly to the generation of electric potential. The uppermost and lowermost regions in the right hand-side of the design domain have no strain, thus both algorithms leave these areas void. From this comparison it follows that the middle regions in the left hand-side of the design domain, close to the substrate, also have low strain and are, therefore, void in Figs. 4b and 5b.

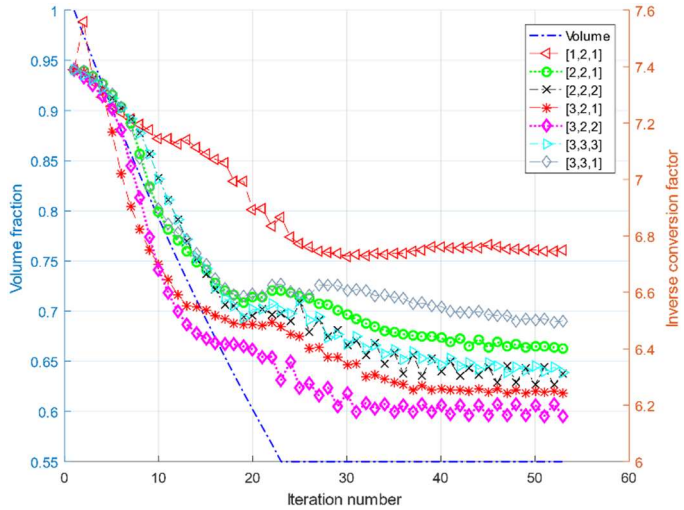

(a) Convergence curves

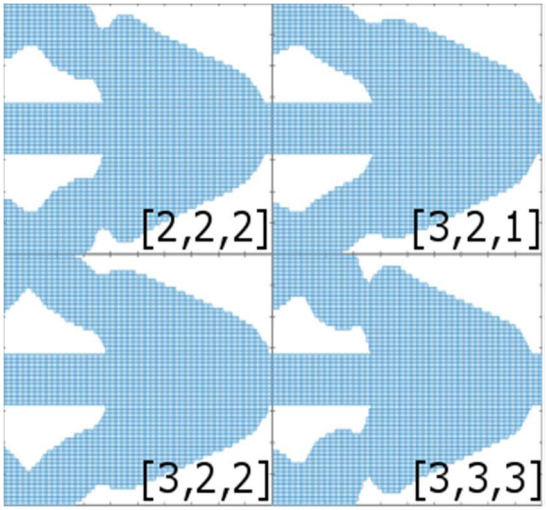

(b) Final topologies for the smallest objective functions.

Fig. 6. Topology optimization results for the piezoelectric harvester described in section 3 with the penalization factors shown in Fig. 6a

3.2 Example 2: Penalization factor analysis

For this example, the optimization was performed with various penalization factor combinations to study their influence in the convergence. The other parameters were kept the same as in section 3.1. Figure 6a exhibits the resulting convergence curve and in Fig. 5a the final topologies for the four lowest final inverse conversion factors are displayed. The penalization factor combinations are written henceforth as $[p_1, p_2, p_3]$.

It can be seen in Fig. 6a that when $p_1 = 3$, where p_1 is the mechanical stiffness' penalization factor, the objective function minimizes more. This is consistent with literature, especially for the compliance minimization of two-dimensional structures [4,6] [9]. Furthermore, after an exhaustive analysis of different penalization factor combinations, not limited to those shown in Fig. 6a, it was found that $p_3 = 1$ and $p_2 = 2$ yield the best results for the optimization. Although the smallest resultant conversion factor was for [3,2,2], as seen in Fig. 6a, its convergence was significantly less stable, thus the chosen penalization factor combination for the succeeding sections was [3,2,1]. Moreover, it was found that the algorithm is considerably more stable when using the sensitivity weight factors as $w_S = 60\%$ and $w_E = 40\%$.

An identical analysis was done considering the equipotential boundaries and its results are presented in Fig. 7. Due to the initial instability caused by the coupling constraints, many of the penalization factor combinations used for Fig. 6 could not be used for Fig. 7.

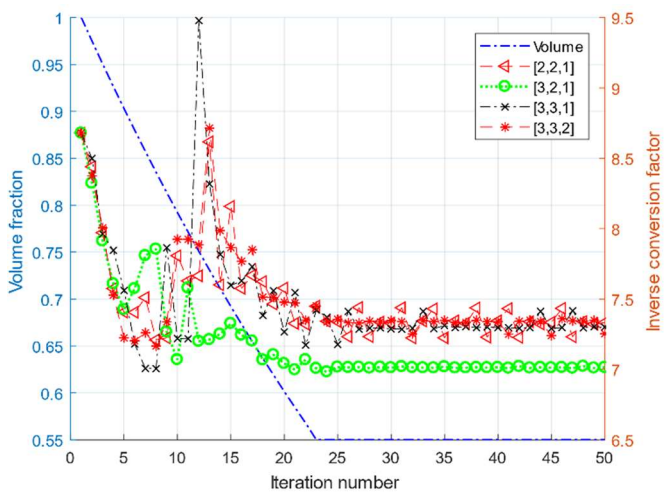

(a) Convergence curves

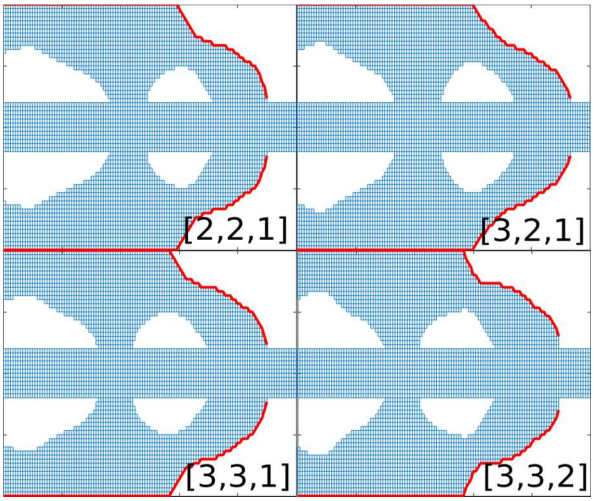

(b) Final topologies for the smallest objective functions.

Fig. 7. Topology optimization results for the piezoelectric harvester described in section 3 with equipotential boundary constraint and the penalization factors shown in Fig. 7a

As can be seen in Fig. 7a, similar to the results obtained in Example 2, the application of the equipotential boundary condition increases the algorithm's instability. Different from the results in Fig. 6a, however, the convergence curves for three penalization factor combinations all converge to around the same value of about 7.3, while the combination [3,2,1] clearly yields the best and, at least from about 25 iterations on, the most stable convergence reaches a 7.01 inverse conversion factor. The voltage difference between the electrodes is 36.16, 33.65, 37.11, and 39.87 mV for the penalization factor combinations of [2,2,1], [3,2,1], [3,3,1], and [3,3,2], respectively. For $F = 1N$, no significant differences is displayed.

4. Harvester Geometric Analysis

In the previous section, the geometric properties were kept the same for both examples and the optimization parameters were varied with [3,2,1], $w_S = 60\%$, and $w_E = 40\%$ to yield the best results. In this section, these parameters are kept constant and geometric characteristics' effects on the optimization algorithm are studied.

4.1 Example 3: Harvester total thickness H analysis

The design domain's geometry is varied to determine its effect on the algorithm's convergence. The length is constant, $L = 100mm$, and the thickness H has three possible values: 20, 40, and $60mm$. The optimization parameters are $ER = 1\%$, $AR = 0.5\%$, and $x_{min} = 1\%$. For all instances, the substrate thickness fraction is $\beta = 20\%$, while the mesh consists of 180 by 90 elements with a $7mm$ filter radius. The results are displayed in Fig. 8. For the $40mm$ and the $60mm$ thick harvesters, the target volume was 55%, as before, but for the $20mm$ thick harvester, the target volume was set to 64%. This change was required in order to guarantee that the objective function only minimizes for the thinner structure since when the piezoelectric volume reaches 64% of the initial volume, there are no more piezoelectric elements with negative sensitivities; in other words, removing them after reaching this volume results in the increase of the inverse conversion factor.

Figure 8a shows that the objective function decreased by 31.3%, 16.2%, and 0.82% for the $60mm$, $40mm$, and the $20mm$ thick beam, respectively. It can be gathered that a greater percentile minimization of the inverse conversion factor can be achieved for thicker piezoelectric harvesters, while thinner ones are inherently more efficient. This supports the production of thinner piezoelectric beam-like structures for a maximum conversion factor if there are no constraints to the harvester's length.

Figure 9 shows the results of an identical analysis done by considering the equipotential boundary constraints. As with the results displayed in Fig. 8, Fig. 9 shows that the initial inverse energy conversion factors of the unoptimized topologies of the thinner harvesters are naturally smaller than that of the thicker ones, yet the percentile reduction of the same factor of the former is smaller than that of the latter when using the topology optimization algorithm presented in this study. More specifically, the percentile reduction of the objective function achieved for the 20, 40, and 60 mm thick harvesters are 8.11%, 19.41%, and 26.80%, respectively.

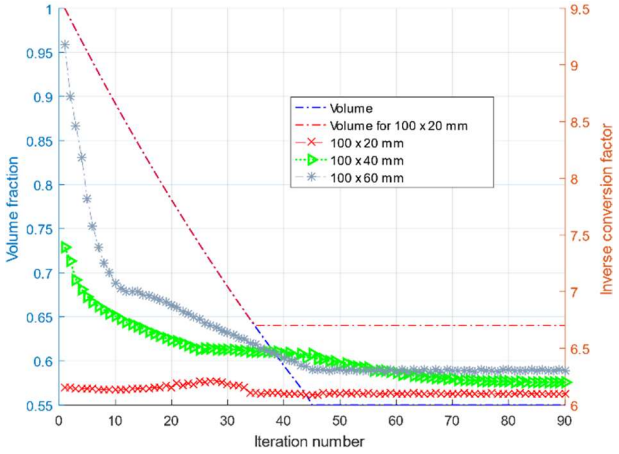

(a) Convergence curves

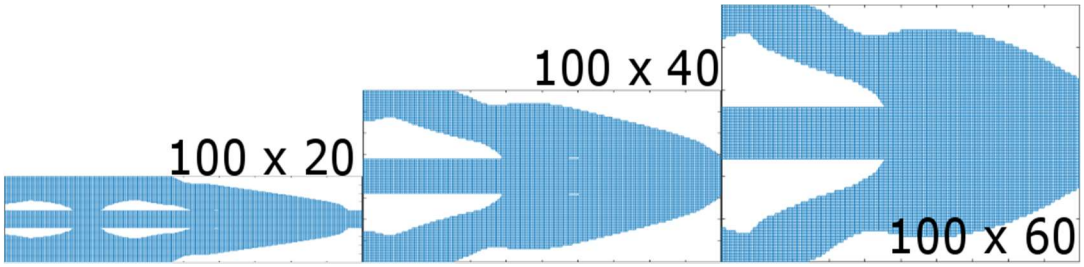

(b) Final topology for different thicknesses

Fig. 8. Topology optimization results for the piezoelectric harvester with different thicknesses

Different from the results found in Fig. 8, and due to the instability caused by the addition of the voltage coupling constraints, the sensitivity weight factors used for 20 and 60 mm thick harvesters were $w_S = 62\%$ and $w_E = 40\%$. Furthermore, the input values of ER and AR were set to 2% and 1%, respectively. The final inverse conversion factors are all around 7.1, about 0.7 greater than the case without the application of the equipotential boundary. Additionally, regarding the optimization code, the voltage differences between the electrodes for the 20, 40, and 60 mm thick harvesters are 101.51, 31.26, and 19.26 mV, respectively. Therefore, considering the proposed objective function and despite having similar inverse conversion factors, the thinner harvester yields a far greater electric potential difference.

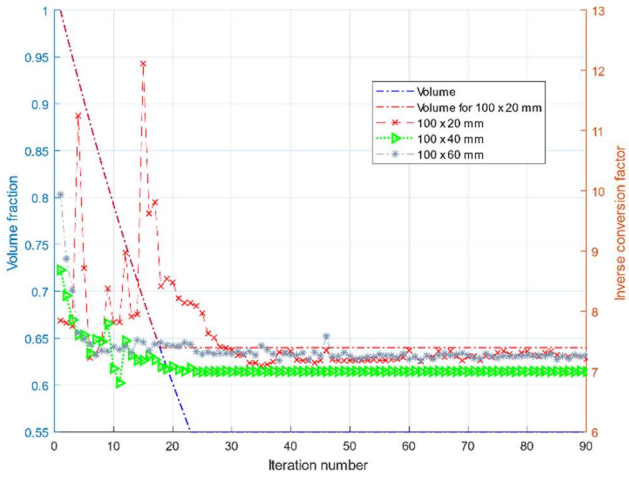

(a) Convergence curves

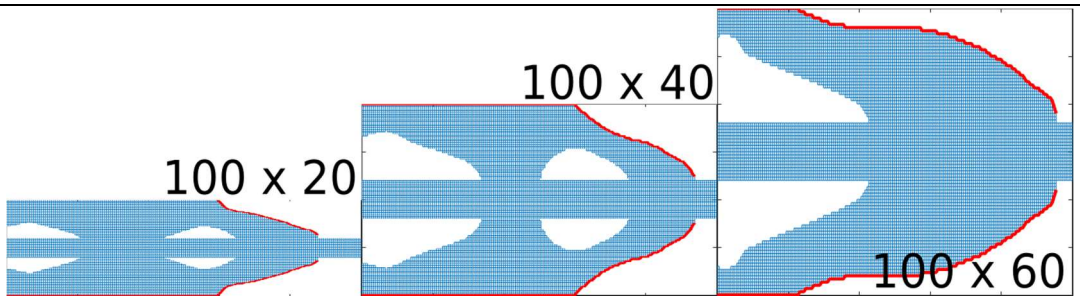

(b) Final topology for different thicknesses.

Fig. 9. Topology optimization results for the piezoelectric harvester with different thicknesses considering equipotential boundary constraints

4.2 Example 4: Substrate thickness percentage β analysis

The influence of the substrate's thickness fraction on the optimization is another geometric characteristic that can be studied. The algorithm is run with various values of β and a harvester with constant thickness $H = 40mm$. The other parameters are identical to those in Example 3. Figure 10 shows the results.

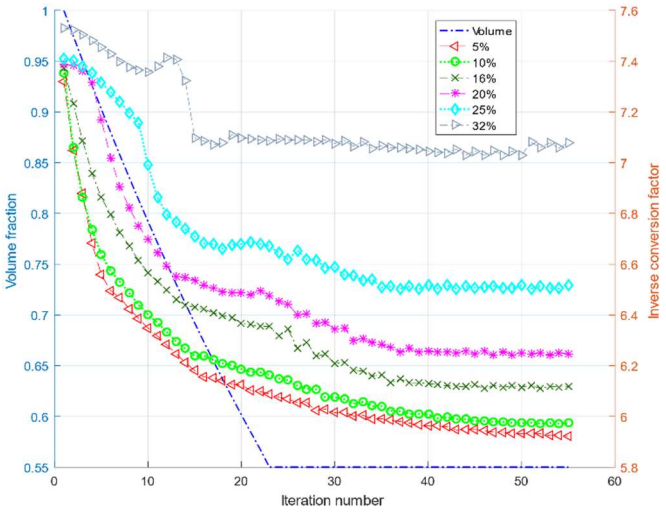

(a) Convergence curves

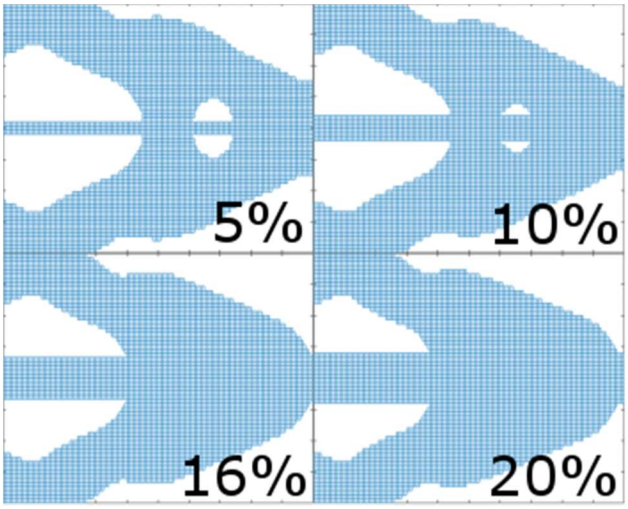

(b) Final topologies for different substrate thickness ratios

Fig. 10. Topology optimization results for the piezoelectric harvester with different substrate thickness ratios

In Fig. 10a, the objective function decreases in 6.0%, 12.0%, 15.5%, 17.0%, 18.8%, and 19.1%, corresponding to the thickness ratios shown in Fig. 10a's legend in descending order. One can conclude that the conversion factor of a piezoelectric harvester is best for thin substrates. This can be useful for manufacturing purposes and can be further empirically studied.

A similar conclusion can be reached after applying the voltage coupling constraints, as can be seen in Fig. 11. According to Fig. 11a, the convergence is unstable in the initial iterations since with the previous cases of the application of the equipotential boundary condition to the analysis and the final inverse conversion factors reached are greater than those shown in Fig. 10a. The voltage differences between the electrodes are 32.91, 31.55, 31.55, 33.65, 34.70, 36.65 mV and β varies from 5% to 32%, as shown Fig. 11a's legend, respectively. In this case, the smaller the substrate fraction, the smaller the inverse conversion factor and the greater the electric potential difference with the exception that the smallest substrate resulted in an intermediate voltage output.

5. Materials Analyses

In the next two Examples, the effect of the energy harvester's materials on the outcome of the optimization algorithm is investigated. The geometric properties are $\beta = 20\%$, $L = 100mm$, and $H = 40mm$ and [3,2,1] is used as the penalization factor combination.

5.1 Example 5: Substrate material analysis

For the metallic substrate, three different materials are considered for the analysis: copper, with Young Modulus of $117GPa$ and 0.33 Poisson coefficient; aluminium, with Young Modulus of $68GPa$ and 0.36 Poisson coefficient; and steel. The piezoelectric material used is PZT-4 and the other optimization parameters are the same as those in Example 1. Figure 12 displays the results of the optimization.

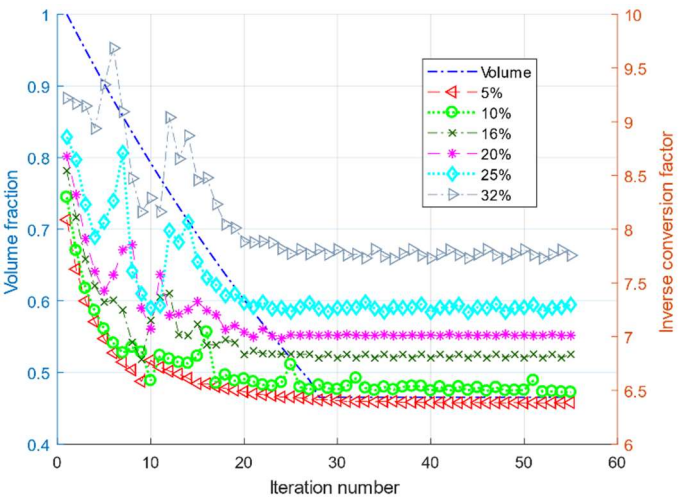

(a) Convergence curves

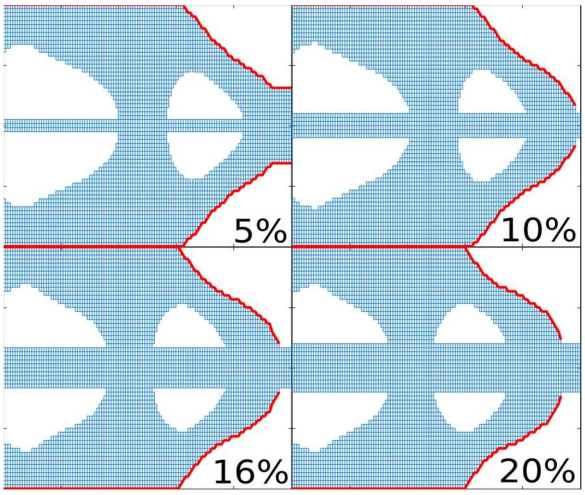

(b) Final topologies for different substrate thickness ratios.

Fig. 11. Topology optimization results for the piezoelectric harvester with different substrate thickness ratios considering equipotential boundary constraints

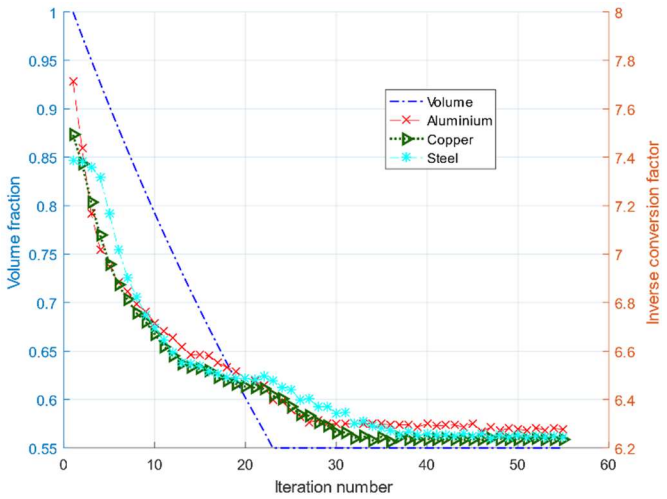

(a) Convergence curves

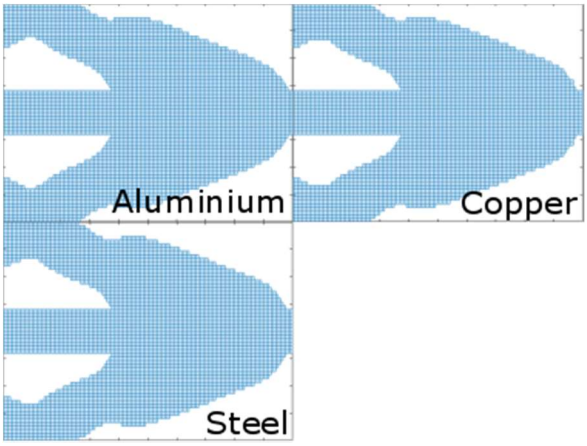

(b) Final topologies for different substrate materials

Fig. 12. Topology optimization results for the piezoelectric harvester with different substrate materials

For the substrate consisting of steel, copper, and aluminium, the resulting inverse conversion factors decreased to 15.5%, 16.8%, and 18.6%, respectively, which can be seen in Fig. 12a. Though, despite this percentile reduction difference, the final values of the objective function are fairly alike. Moreover, the final topologies for the different materials are practically the same, as can be seen in Fig. 12b.

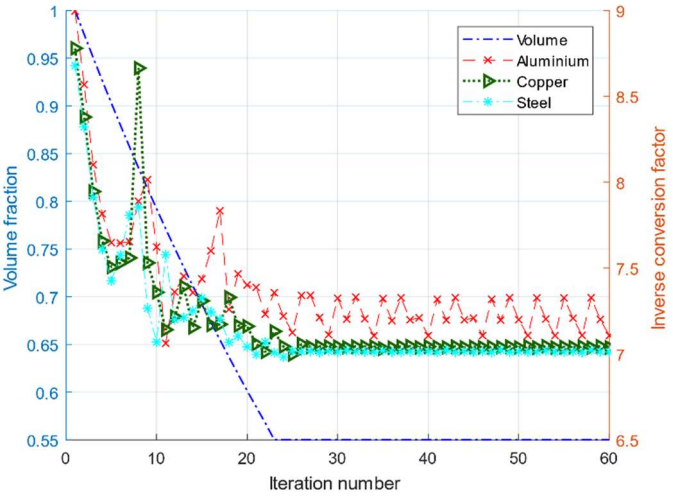

(a) Convergence curves

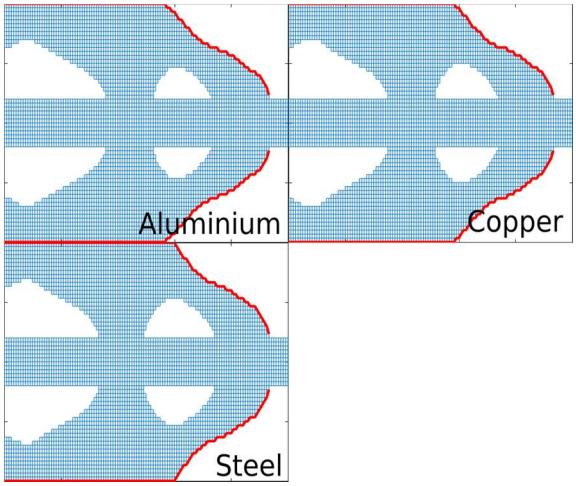

(b) Final topologies for different substrate materials.

Fig. 13. Topology optimization results for the piezoelectric harvester with different substrate materials considering equipotential boundary constraints

After applying the voltage coupling constraints to the electrodes, the topologies shown in Fig. 13b are also similar to one another. By displaying a void region in the middle-right section of the harvester, it can be seen that the final inverse conversion factors shown in Fig. 13a are greater than those displayed in Fig12a. Due to the greater instability of the convergence for the aluminium substrate, the sensitivity weight factor used for it was $w_S = 62\%$ and $w_E = 40\%$. The percentage reduction of the objective function for aluminium, copper, and steel was 21.00%, 19.84%, and 19.21%, respectively, although the final value was approximately the same and about 7.02. The electric potential differences between the electrodes were 36.60, 34.97, and 33.65 mV, respectively for an input force of $F = 1N$. Therefore, as can be seen from Fig. 13a, both the electric potential difference and the final inverse conversion factor do not vary significantly when changing the substrate material. Note however, that the convergence curve for aluminium was significantly unstable despite using a greater value of w_S.

5.2 Example 6: Piezoelectric material analysis

In this last Example, three different materials are used for the piezoelectric domain: PZT-5H, PZT-5A, and PZT-4, the properties of which are provided in Table 1. The optimization parameters and the substrate material are the same as in Example 1. Figure 14 displays the results.

As can be seen in Fig. 14a and through the algorithm's code, the inverse conversion factor decreases in 13.8% for PZT-5A, 15.5% for PZT–4, and 19.3% for PZT-5H. But in absolute value, the final objective function using each material is significantly different from each other. For example, using PZT-4, the optimized inverse conversion factor is 2.53 which is better than when using PZT-5H, while the same factor is 0.61 which is better when using PZT-5A in comparison to when using PZT-4. The final topologies are displayed in Fig. 14b and they appear to be quite similar to one another, with the exception of PZT-5H, which seems to concentrate material near the clamped boundary.

Table 1. PZT-5A and PZT-5H material properties

Properties	PZT-5A	PZT-5H
$\mathbf{e}\ [C/m^2]$	$\begin{bmatrix} 0 & 0 & -5.36 \\ 0 & 0 & -5.36 \\ 0 & 0 & 15.78 \\ 0 & 12.29 & 0 \\ 12.29 & 0 & 0 \\ 0 & 0 & 0 \end{bmatrix}$	$\begin{bmatrix} 0 & 0 & -6.62 \\ 0 & 0 & -6.62 \\ 0 & 0 & 23.24 \\ 0 & 17.03 & 0 \\ 17.03 & 0 & 0 \\ 0 & 0 & 0 \end{bmatrix}$
$\mathbf{c}^E\ [10^2 GPa]$	$\begin{bmatrix} 1.21 & 0.754 & 0.752 & 0 & 0 & 0 \\ 0.754 & 1.21 & 0.752 & 0 & 0 & 0 \\ 0.752 & 0.752 & 1.11 & 0 & 0 & 0 \\ 0 & 0 & 0 & 0.211 & 0 & 0 \\ 0 & 0 & 0 & 0 & 0.211 & 0 \\ 0 & 0 & 0 & 0 & 0 & 0.226 \end{bmatrix}$	$\begin{bmatrix} 1.27 & 0.802 & 0.847 & 0 & 0 & 0 \\ 0.802 & 1.27 & 0.847 & 0 & 0 & 0 \\ 0.847 & 0.847 & 1.15 & 0 & 0 & 0 \\ 0 & 0 & 0 & 0.230 & 0 & 0 \\ 0 & 0 & 0 & 0 & 0.230 & 0 \\ 0 & 0 & 0 & 0 & 0 & 0.235 \end{bmatrix}$
$\boldsymbol{\varepsilon}^S\ [nF/m]$	$\begin{bmatrix} 8.14 & 0 & 0 \\ 0 & 8.14 & 0 \\ 0 & 0 & 7.32 \end{bmatrix}$	$\begin{bmatrix} 15.1 & 0 & 0 \\ 0 & 15.1 & 0 \\ 0 & 0 & 12.7 \end{bmatrix}$

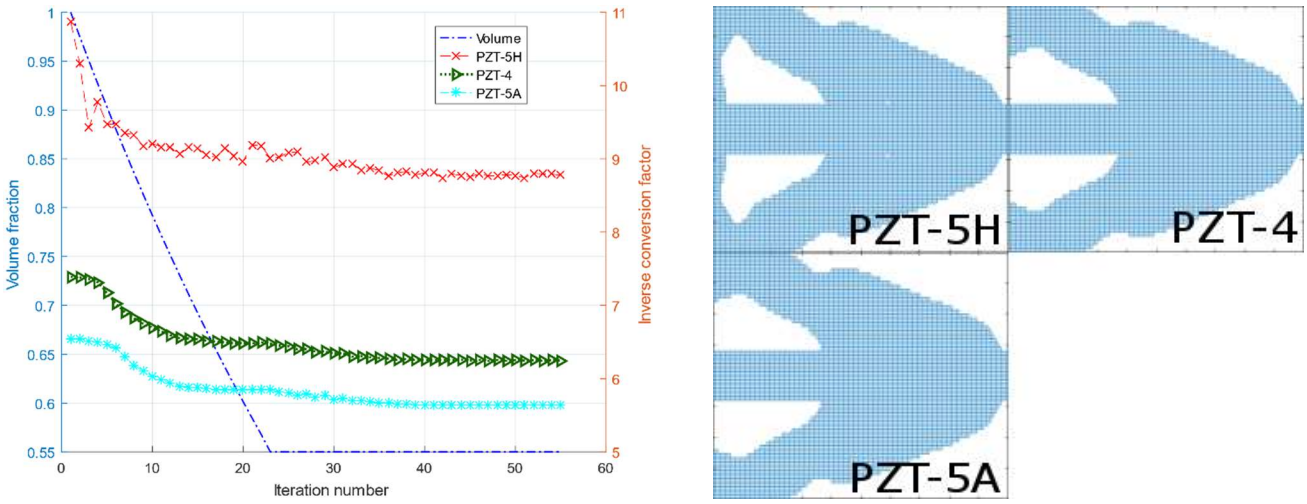

(a) Convergence curves **(b)** Final topologies for different piezoelectric materials

Fig. 14. Topology optimization results for the piezoelectric harvester with different piezoelectric materials

The results obtained in Fig. 14 are qualitatively similar to the ones obtained in Fig. 15, in which the equipotential boundary

constraint was applied, that is, the final inverse conversion factor is smaller for PZT-5A than for PZT-4 which, in turn, is smaller than for PZT-5H, with final values of 9.99, 7.0, and 6.34, respectively. The topologies obtained in Fig. 15b are different than those in Fig. 14b, but similar to the resulting optimal topologies obtained in the previous examples when the equipotential voltage constraint is applied. In contrast to the higher inverse conversion factor, the harvester with PZT-5H yielded a 51.33 mV difference between the electrodes, while the electric potential difference for the harvesters with the other piezoelectric materials yield about 34 mV, all for a $1N$ force.

It can be seen in Figs. 12 and 13 that the final value of the objective function does not vary significantly when using different substrate materials and considering Figs. 14 and 15, it can be concluded that PZT-5A is the most advantageous material for the piezoelectric domain of the harvester since it yields a smaller inverse conversion factor.

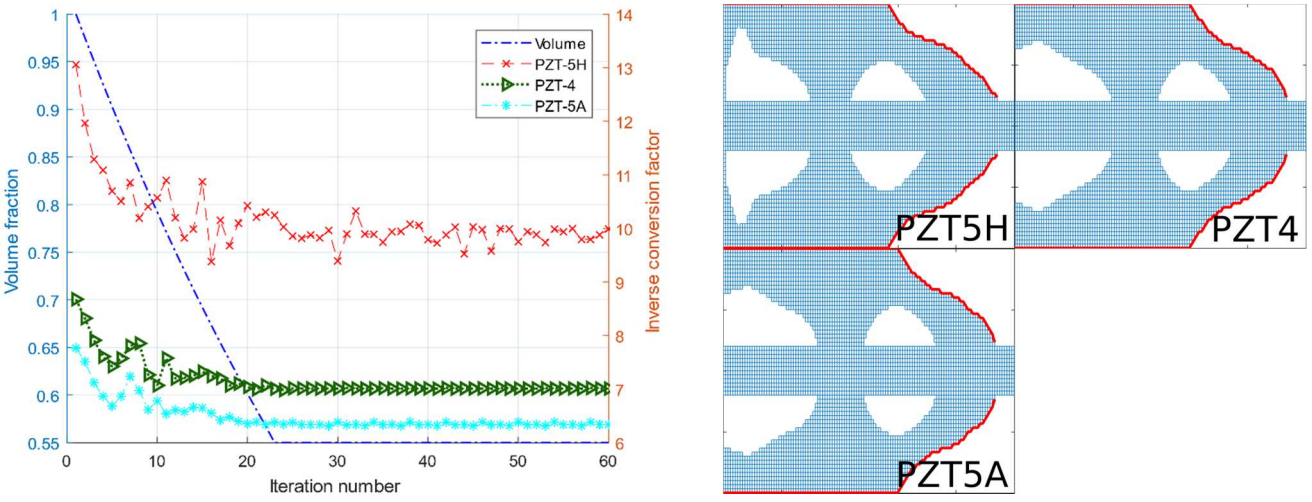

(a) Convergence curves

(b) Final topologies for different piezoelectric materials

Fig. 15. Topology optimization results for the piezoelectric harvester with different piezoelectric materials considering equipotential boundary constraints

6. Conclusions

A beam-like bimorph piezoelectric harvester with a series connection of the piezoelectric layers was modeled in two dimensions using a FE, the plane strain hypothesis, and the open-circuit conditions. The model was then implemented and its topology was optimized using the proposed multiparameter method to minimize the inverse energy conversion factor. Each physical property of the piezoelectric material has a distinct material law penalization factor which was varied in order to determine the combination that yields the best convergence for the iterative optimization procedure. The results for the harvester without electrodes and the harvester with the equipotential boundary applied are displayed in Figs.6 and 7, respectively. Considering the minimization of the inverse conversion factor as well as the convergence stability, the best combination was found to be [3,2,1].

Further topology optimizations of the harvester were performed to study how the geometric parameters affect the convergence. First, an analysis of the thickness to length ratio was performed while considering a fixed substrate thickness fraction and the results are displayed in Figs. 8 and 9. In Figs. 10 and 11, the results of the topology optimization algorithm considering fixed length L and thickness H while varying the substrates thickness are provided. It can be seen that thinner substrates yield harvesters with a better energy conversion factor and a high output voltage. Additionally, the implemented algorithm seems be more effective at minimizing the inverse conversion factor of thicker harvesters in a relative sense, although thinner harvesters tend to naturally be more efficient in producing electric energy from strain energy.

Finally, the dependence of the implemented optimization method's convergence on the type of material was studied and the results considering different substrate materials are shown in Figs. 12 and 13. The method seems to be more efficient in minimizing the inverse conversion factor for less stiff materials although it does not alter significantly its value when reaching the optimized topology. On the other hand, the voltage difference between the electrodes also remains approximately the same. Furthermore, the piezoelectric material PZT-5A yields the best convergence factor although PZT-5H yields the best output voltage for the case considered.

By comparing the results of all studied examples with and without the electrodes, it can be seen that the addition of the voltage coupling constraint, as shown in Eq. (6), effectively decreases the electrical energy to input force's work ratio, or rather, increases its inverse value ζ in the objective function as shown in Eq. (7). Since, to the best of the author's knowledge, this has not been extensively researched, it is important to study in future works how the position or length of the electrodes influences the objective function and the output voltage.

The results shown in this study are beneficial to understand how the topology optimization algorithm for piezoelectric harvesters subjected to a static load using a multiparameter discrete method works when being optimized in the thickness direction. Future projects will be done to consider the influence of coupled Eq. (6) on the topology and the model can further be extended to three dimensions. The development of AM techniques may enable the manufacturing of more complex geometries,

even allows the analysis of composite piezoelectric energy harvesting devices.

Acknowledgments

The authors are grateful to FAPESP (São Paulo Research Foundation grant numbers 2013/08293-7 and 2018/00075-4) and CAPES (Coordination for the Improvement of Higher Education Personnel) for the financial support of this work.

Conflict of Interest

The authors declare no conflict of interest.

Nomenclature

A	Cross-section area [m^2]	$\boldsymbol{u}$	Displacement vector [m]
$[B]$	Shape function derivative matrix	w_E	Electric sensitivity weight factor
$\mathbf{c}^{\mathbf{E}}$	Elastic tensor [N]	w_S	Strain sensitivity weight factor
$\boldsymbol{D}$	Electric displacement vector [C/m^2]	x	Element density
$\boldsymbol{E}$	Electric field vector [N/C]	α	Sensitivity
$\mathbf{e}$	Piezoelectric coupling tensor [C/m^2]	β	Harvester substrate thickness fraction
$\boldsymbol{F}$	Force vector [N]	Γ	Domain boundary
H	Linear shape function	$\boldsymbol{\varepsilon}^{\mathbf{S}}$	Dielectric permittivity tensor [F/m]
J	Jacobian	ϵ	Strain
$\boldsymbol{K}$	Mechanical stiffness matrix [N/m^2]	ζ	Inverse energy conversion factor
$\boldsymbol{l}$	Lagrange nodal coupling vector	$\boldsymbol{\Lambda}$	Lagrange coupling matrix
n	Unit vector normal to an area	$\boldsymbol{\lambda}$	Adjoint displacement vector [m]
p	Penalization factor	$\boldsymbol{\mu}$	Adjoint electric potential vector [V]
$\boldsymbol{Q}$	Electric charge vector [C]	Π^{E}	Electric energy [J]
r	Filter radius [m]	Π^{S}	Strain energy [J]
$\boldsymbol{S}$	Strain vector	σ	Stress [N/m^2]
$\boldsymbol{T}$	Stress vector [N/m^2]	$\boldsymbol{\phi}$	Electric potential [V]
T_r	Traction vector	Ω	Domain area

References

[1] Lippmann, G., Principe de la conservation de l'électricité, ou second principe de la théorie des phénomènes électriques, *Journal de Physique Théorique et Appliquée*, 10(1) (1881) 381-394.
[2] Erturk, A., Inman, D. J., *Piezoelectric Energy Harvesting*, John Wiley & Sons, 2011.
[3] Nelli Silva, E. C., Kikuchi, N., Design of piezocomposite materials and piezoelectric transducers using topology optimization-Part III, *Archives of Computational Methods in Engineering*, 6(4) (1999) 305-329.
[4] Bendsoe, M. P., Sigmund, O., *Topology Optimization: Theory, Models, and Aplications*, Springer, 2013.
[5] Steven, G. P., Xie, Y. M., *Evolutionary Stuctural Optimization*, Springer, 2014.
[6] Huang, X., Xie, M., *Evolutionary Topology Optimization of Continuum Structures: Methods and Applications*, Wiley, 2010.
[7] Vicente, W. M., Picelli, R., Pavanello, R., Xie, Y. M., Topology optimization of frequency responses of fluid-structure interaction systems, *Finite Elements in Analysis and Design*, 98 (2015) 1-13.
[8] Azevedo, F., Picelli, R., Vicente, W., Pavanello, R., A bi-directional evolutionary topology optimization method applied for acoustic mufflers design, *EngOpt 5th International Conference on Engineering Optimization*, Iguassu Falls, Brazil, 2016.
[9] Picelli, R., Vicente, W. M., Pavanello, R., Xie, Y. M., Evolutionary topology optimization for natural frequency maximization problems considering acoustic-structure interaction, *Finite Elements in Analysis and Design*, 106 (2015) 56-64.
[10] Sigmund, O., Torquato, S., Aksay, I. A., On the design of 1-3 piezocomposites using topology optimization, *Journal of Materials Research*, 13(4) (1998) 1038-1048.
[11] Carlos Emilio Nelli Silva, Ono Fonseca, J. S., de Espinosa, F. Montero, Crumm, A. T., Brady, G. A., Halloran, J. W., Kikuchi, N., Design of piezocomposite materials and piezoelectric transducers using topology optimization-Part I, *Archives of Computational Methods in Engineering*, 6(2) (1999) 117-182.
[12] Donoso, A., Sigmund, O., Optimization of piezoelectric bimorph actuators with active damping for static and dynamic loads, *Structural and Multidisciplinary Optimization*, 38(2) (2008) 171-183.
[13] Zheng, B., Chang, C.-J., Gea, H. C., Topology optimization of energy harvesting devices using piezoelectric materials, *Structural and Multidisciplinary Optimization*, 38(1) (2008) 17-23.
[14] Noh, J. Y., Yoon, G. H., Topology optimization of piezoelectric energy harvesting devices considering static and harmonic dynamic loads, *Advances in Engineering Software*, 53 (2012) 45-60.
[15] Lin, Z. Q., Gea, H. C., Liu, S. T., Design of piezoelectric energy harvesting devices subjected to broadband random vibrations by applying topology optimization, *Acta Mechanica Sinica*, 27(5) (2011) 730.

[16] Kiyono, C. Y., Silva, E. C. N., Reddy, J. N., Optimal design of laminated piezocomposite energy harvesting devices considering stress constraints, *International Journal for Numerical Methods in Engineering*, 105(12) (2016) 883-914.
[17] Chen, Z., Song, X., Lei, L., Chen, X., Fei, C., Chiu, C. T., Qian, X., Ma, T., Yang, Y., Shung, K., Chen, Y., Zhou, Q., 3D printing of piezoelectric element for energy focusing and ultrasonic sensing, *Nano Energy*, 27 (2016) 78-86.
[18] Kim, K., Zhu, W., Qu, X., Aaronson, C., McCall, W. R., Chen, S., Sirbuly, D. J., 3D Optical Printing of Piezoelectric Nanoparticle-Polymer Composite Materials, *ACS Nano,* 8(10) (2014) 9799-9806.
[19] Bodkhe, S., Turcot, G., Gosselin, F. P., Therriault, D., One-Step Solvent Evaporation-Assisted 3D Printing of Piezoelectric PVDF Nanocomposite Structures, *ACS Applied Materials & Interfaces*, 9(24) (2017) 20833-20842.
[20] IEEE Standard on piezoelectricity, ANSI/IEEE Std 176-1987, 1988.
[21] Cook, R. D., Malkus, D. S., Plesha, M. E., Witt, R. J., *Concepts and applications of finite element analysis*, Wiley, 2001.